Combustion and Flame 234 (2021) 111641

Contents lists available at ScienceDirect

Combustion and Flame

journal homepage: www.elsevier.com/locate/combustflame

The evolution of pressure gain in turbulent fast flames

Hardeo M. Chin[a], Jessica Chambers[a], Jonathan Sosa[b], Alexei Poludnenko[c,d], Vadim N. Gamezo[e], Kareem A. Ahmed[a,*]

[a] *Propulsion and Energy Research Laboratory, Center for Advanced Turbomachinery & Energy Research, Department of Mechanical and Aerospace Engineering, University of Central Florida, Orlando, FL 32816, United States*
[b] *Naval Center for Space Technology, Naval Research Laboratory, Washington, DC 20375, United States*
[c] *Department of Mechanical Engineering, University of Connecticut, Storrs, CT 06269, United States*
[d] *Department of Aerospace Engineering, Texas A&M University, College Station, TX 77843, United States*
[e] *Laboratories for Computational Physics and Fluid Dynamics, Naval Research Laboratory, Washington, DC 20375, United States*

ARTICLE INFO

Article history:
Received 1 May 2021
Revised 21 July 2021
Accepted 22 July 2021
Available online 9 August 2021

Keywords:
Pressure gain combustion
Rankine-hugoniot analysis
Deflagration-to-detonation transition
Turbulent fast flames

ABSTRACT

This research quantifies the evolution of pressure for fast burning regimes characterized by various degrees of compressibility and involving turbulent flames and shocks. The experimental exploration is conducted in a Turbulent Shock Tube facility, where the level of flame compressibility is controlled by varying the equivalence ratio of the hydrogen-air mixture. High-speed particle image velocimetry, chemiluminescence, schlieren, and pressure measurements are simultaneously acquired to capture the rise in stagnation pressure for various regimes from fast flames to shock-flame complexes. The pressure and velocity measurements are used to analyze combustion regimes on the Rankine-Hugoniot diagram that shows the flame-driven compression for a range of fast flame conditions evolving toward detonation onset. Various levels of compression are dependent on the level of shock-flame coupling and flame velocities. Lower degrees of compressibility show 52% efficiency of an ideal ZND cycle with 40% thermal efficiency, while shock-flame complexes are shown to produce 81% of the work produced by an ideal ZND cycle with 53% thermal efficiency.

1. Introduction

While any combustion process that produces an increase in stagnation pressure can be characterized as pressure-gain combustion (PGC), this technical term usually refers to free-flow combustion or specific types of combustors for propulsion applications, and excludes combustion in mechanically confined systems, such as piston engines. Pressure gain combustion is a highly desired form of combustion for propulsion applications due to the higher thermodynamic efficiency, potential for reduced emissions, and thrust capability [1]. There are various ongoing studies characterizing PGC devices in the form of rotating detonation engines (RDE) [2-7] and pulse detonation engines (PDE) [8-11]. These detonation-based engines exhibit rapid burning rates, which may result in more compact and efficient propulsion systems. However, the unsteady nature of detonation-based cycles presents a significant challenge for practical implementation, system integration, and characterization [1]. One of the outstanding challenges is the quantification of pressure gain for a given burning mode, whether it is a detonation, or other supersonic burning regimes, such as a fast flame or a shock-flame complex. Quantifying pressure gain requires simultaneous measurements of velocity, static pressure, temperature, and knowledge of the gas composition. Experimental measurements of each of these parameters have been independently explored [3,12-15], but an accurate and reliable measurement of pressure gain is still yet to be achieved. Quantifying the total pressure rise for these systems is crucial prior to assessing the potential performance and thrust benefits that can be obtained from the integration of a PGC device in a propulsion system.

The complex nature of PGC devices causes them to operate in a regime between constant volume and constant pressure combustion. The thermodynamic cycle characteristics of a detonation are similar to those of constant volume combustion, where the heat addition process is tied to a pressure increase on the pressure-specific volume (P-v) diagram [1]. However, the question still remains of how transient fast flame regimes behave. These regimes

---

[*] Corresponding author.
E-mail addresses: Hardeo28@knights.ucf.edu (H.M. Chin), Jessica.Chambers7@knights.ucf.edu (J. Chambers), Jonathan.Sosa@nrl.navy.mil (J. Sosa), Alexei.Poludnenko@uconn.edu (A. Poludnenko), Kareem.Ahmed@ucf.edu (K.A. Ahmed).

https://doi.org/10.1016/j.combustflame.2021.111641

may occur when the operating conditions are not ideal, and the detonations may periodically fail and reignite. There have been observations of fast flames generating pressure rise before detonation onset in experiments and numerical simulations [13,16-18]. This pressure rise resulted from the intrinsic instability of premixed turbulent flames that pulsate and generate pressure waves, when the flame burning speed approaches the Chapman-Jouguet (CJ) deflagration velocity during a pulsation. The pressure build-up may eventually lead to the deflagration-to-detonation transition through the runaway mechanism described in [19-21].

From a thermodynamic perspective, Vitutthivithayarak et al. examined the differences between the constant-volume Humphrey cycle, the Fickett-Jacobs (FJ) cycle based on the CJ detonation model, and the Zeldovich-von Neumann-Döring (ZND) cycle [22]. The Humphrey and FJ cycles do not take into account the energy increase due to shock compression, only considering heat addition. The ZND cycle is based on the detonation flow physics, where a shockwave compresses the material to the ZND state on the inert Hugoniot curve and the exothermic chemical reactions bring the process to the equilibrium Hugoniot curve. The P-ν diagram representing the ZND cycle is still an approximation since it assumes that shock compression proceeds along the inert Hugoniot, and the expansion producing useful work starts at the ZND point. If the P-ν diagram is plotted using static pressures, then it also does not consider the kinetic energy of the material in the detonation wave. Nevertheless, the ZND cycle is considered more accurate in representing detonations than Humphrey and FJ cycles and is often used to analyze the thermodynamic efficiency of detonations. It is important to note that the Humphrey and FJ cycles are thermodynamic cycles, which deal with the complete system, whereas the ZND cycle focuses solely on the combustion process. Thus, we model the fast flames presented in this work based on the ZND cycle which focuses on the combustion process and not the complete system.

An early study by Oppenheim modeled transient DDT stages by developing the Q-curve, which represents the locus of post-flame states [23]. Similarly, Troshin performed a Hugoniot analysis of several modes of deflagration [24]. Akin to Oppenheim, Troshin found that an equilibrium adiabatic Hugoniot curve was insufficient to describe the propagation of an unsteady double discontinuity [24]. Therefore, to model these fast flames, which contain a double discontinuity (decoupled shock and flame), two Hugoniot curves must be used: an inert and equilibrium Hugoniot. Recent studies that performed this modeling analysis have been mostly computational in nature. Nordeen et al. performed numerical simulation of an RDE and saw that their P-ν diagram based on the velocity field pathlines agreed with the general model of the ZND detonation [14]. Schwer and Kailasanath also did a numerical investigation of RDEs and observed that the thermodynamic cycles for different pathlineswere geometrically independent of the engine location [2,25]. Kaemming and Paxon used a different computational and experimental approach to estimate the total pressure gain in an RDE using Equivalent Available Pressure (EAP) [12]. Their method derives the ideal EAP (EAPi) by computing the stagnation pressures at the inlet, combustor entrance, combustor exit, and calculating the net pressure gain across these components. They compared these values with experimental gross thrust measurements at the combustor exit. Using the thrust equation, they were able to calculate stagnation pressure and actual EAP. For most of their cases, the computational and experimental EAP differences ranged from 1.7% to 8.7%. For combustors operating with small overall pressure ratios and high loss inlets, the EAP was 15% below EAPi.

From an experimental standpoint, thermodynamic analysis requires simultaneous pressure, velocity, temperature, and composition measurements, which are difficult to obtain. There is currently a lack of experimental data characterizing stagnation pressure rise in fast flames. Recent advances in experimental diagnostics have provided higher-resolution measurements for this analysis. Velocity measurements can be acquired through particle image velocimetry (PIV), which requires consideration of the seed particle size, field of view, laser sheet, and timing. Implementing PIV in RDEs becomes challenging due to their geometrically complex configurations [5,26,27]. Measuring static pressure is also challenging due to sensor survivability in the high temperature environments, which causes thermal drift, and the need for accurate readings at high temporal resolutions [13,28]. Temperature measurements have been challenging due to high temperatures behind the detonation front. Recent advances in diagnostics have utilized tunable diode laser absorption-spectroscopy (TDLAS) for high-resolution temperature measurements. This measurement technique consists of passing vertical-cavity surface-emitting laser beams (VCSEL) through the points of interest and collecting these beams using a fiber optic [3,29,30]. The actual measurement, however, represents an integrated line-of-sight value and not a point measurement. By measuring the H_2O absorption, the temperature can be calculated at discrete points in the flow field. TDLAS measurements still lack the temporal resolution to capture the rapid transient and extreme gas conditions caused by detonative events. Measurements also become noisy at post-detonation temperatures, and thus the calibration becomes less reliable when converting absorption values to temperature. In this work, temperature is not measured, and instead it is calculated based on gas dynamic equations for the equilibrium Hugoniot using other known thermodynamic properties, such as pressure and velocity.

Since RDEs and PDEs are systems, they may contain inlet and exhaust components that participate in the overall work or thrust production. Generally, for these systems, the entire thermodynamic cycle is analyzed for the pressure gain. However, in this study, we focus on the specific thermodynamic cycle analysis of the supersonic combustion regimes. Flame compressibility results in a pressure rise, which is a key fluid dynamic aspect of this combustion process. Thus, pressure gain in this paper is attributed to a stagnation pressure increase as a result of the turbulent fast flame process and not from a system perspective.

This paper presents the analysis of the evolution of pressure gain for several flame regimes ranging from low compressibility to high compressibility, through experimentation in a Turbulent Shock Tube facility. The flow field for various propagation regimes of a turbulent fast flame is characterized using schlieren, simultaneous high-speed PIV, chemiluminescence, and pressure transducers. Schlieren is used to highlight key features within the flow before detonation onset occurs, such as the decoupled shock-flame structure, and compressed region adjacent to the flame. Velocity and pressure traces are used to quantify the flow-field behavior as these fast flames transition toward detonation. An approach for computing the pressure gain using velocity and pressure is discussed for these fast flames and shock-flame complexes. The traces are then characterized further and plotted on a Rankine-Hugoniot diagram to be compared with the theoretical Hugoniot curves.

2. Experiment and diagnostics

2.1. Experimental facility

Figure 1 shows a schematic of the Turbulent Shock Tube (TST) facility. The TST is used to explore flame regimes from slow deflagrations to detonations. The semi-confined facility has a constant square cross-section of 45 × 45 mm^2 and includes a 125 mm long test section with full optical access designed to sustain detonation pressures and temperatures for laser diagnostics.

The turbulence generator contains a series of perforated plates with a 58% open area, with the last perforated plate located at

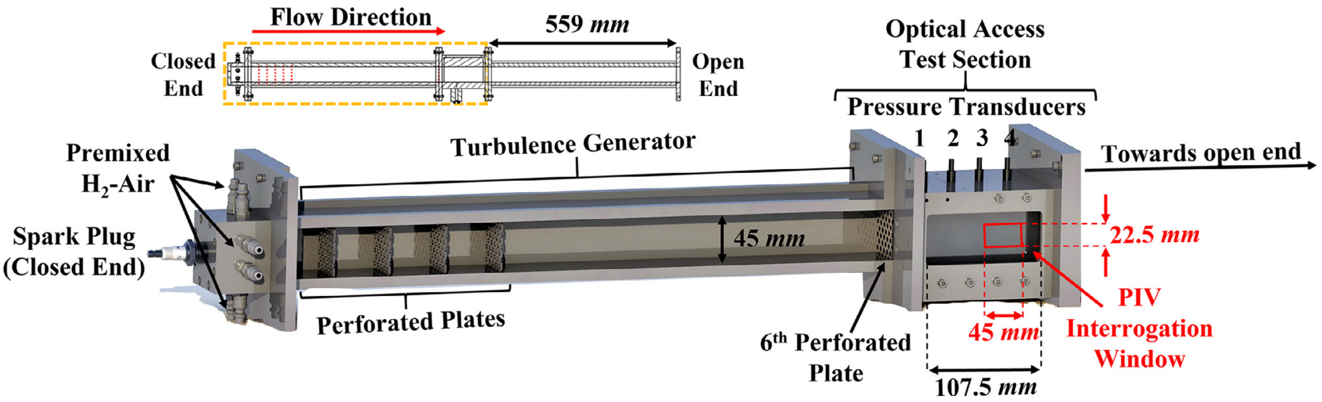

Fig. 1. Schematic of experimental facility.

550 mm from the closed end, just before the test section. This geometric configuration was the result of extensive experimental testing to achieve the desired flame-turbulence conditions [21,31,32]. A spark plug is mounted at the center axis of the channel at the closed end.

2.2. Flow control

A timed control system was used to produce a homogenous mixture of hydrogen and air before ignition. Premixed hydrogen and air are issued into the facility at low flow rates at atmospheric pressure and room temperature to mitigate flow perturbations in the channel. The fuel and air mixture flow rates are controlled to attain the desired equivalence ratio in the range $\Phi = 0.84 - 1.05 \pm 0.011$. Air is directed through a SMC Pneumatics #AW20-N02E-CZ pressure regulator and then into a Dwyer VFA-6-BV flowmeter. Compressed hydrogen gas is regulated and controlled using a Specialty gases Southeast Inc. #HP-702-125-000-A regulator and a Dwyer VFA-3-BV flow meter. The air and fuel flow rates vary in the ranges $28 - 30 \pm 0.25$ *SCFH* and $2.85 - 3.1 \pm 0.054$ *SCFH*, respectively. The hydrogen flow rate is corrected for use on an air calibrated flowmeter ($CFH_{H2} \bullet 0.26 = SCFH_{H2}$); both hydrogen and air lines merge to premix in one line, which is fed to the closed end of the facility. The premixed fuel-air mixture is fed through a solenoid valve into the closed end of the facility for the fill stage. A BNC Model 575 Pulse/Delay Generator was used to trigger the valve and initiate the spark plug.

2.3. Experimental procedure

To initiate the facility operation, fuel and air lines are opened and set to the desired flow rates based on the equivalence ratio of interest. After a 20 s premixed-reactants fill time, a signal triggers the 3-way solenoid valve to stop the mixture flow into the tube. Afterwards, a 4 s wait time allows the mixture to settle, and a signal triggers the coil and spark plug. The spark-ignited flame near the closed end propagates through a series of perforated plates, accelerates, and generates a shock wave that travels ahead of the flame. As the shock passes through the final perforated plate, it creates a highly turbulent, heated, but unreacted flow field. The flame follows the shock and passes through the last plate as an array of sonic jets that interact with the turbulent background flow and create highly turbulent burning conditions downstream of the plate. Depending on the equivalence ratio, a decoupled shock-flame structure, coupled shock-flame complex or detonation will be seen in the test section window.

2.4. Diagnostics

The measurement approach was utilized and documented in previous work [21,31,32]. Schlieren diagnostics are used to observe the general characteristics of the regime of interest within the test section domain. A standard Schlieren Z formation is set up using two 150 mm diameter parabolic mirrors with focal lengths of 1.52 m. A Photron Fastcam SA-Z camera with 1024 × 1024-pixel spatial resolution and a 16-bit range depth captures images at a recording rate of 100 *kfps* with a resolution of 640 × 280 *pixels*. A Nikon lens of focal length 200 mm and $f/2.8$ is used. The camera captures the entire viewing window with the spatial resolution of 175 $\mu m/px$ that corresponds to the pixel-based velocity uncertainty of ±5.6 m/s [21,31].

Pressure transducers are lined along the test section to capture the pressure profile, resolve shock strength and velocity, and acquire the static pressure profiles for the turbulent flame regimes [21,31]. A series of four pressure transducers PCB Model #113B26 are lined along the test section at intervals of 25 mm. The response time for the transducers is $<$ 1 microsecond. The transducers have a sensitivity of 10 mV/psi, and the data is acquired at a frequency of 250 kHz to resolve the post-shock pressure ahead of the flame. When considering the non-linearity and sensitivity variation, the resolved static pressure values have an uncertainty of ±0.17 *atm* ($\pm$ 0.011 P/P_{CJ}). The transducers are connected to a PCB signal conditioner 482C Series to amplify the voltage signals and then are routed to a National Instruments DAQ device coupled with LabVIEW control hardware and software. The pressure measurements are conducted simultaneously with high-speed PIV and OH^* measurements [21,31].

High-speed PIV was setup to quantify the local flow-field velocity. A Nd:YAG Lee LDP Dual Head Laser (532 nm, 25 mJ) is operated at 40 kHz. The laser sheet is set at the center of the test section. The premixed flow is seeded with 0.2 μm Al_2O_3 particles [33]. A Photron Fastcam SAZ camera equipped with a Nikon 50 mm and f/1.2 is used for the 40 kHz PIV. The PIV image resolution is 42 μm/pix and processed using DaVis software with 30 step multi-pass method ending with a 16 × 16 pixel interrogation window and a 75% overlap. This results in a measurement scale $\lambda_m = 168$ μm for a field of view of 44 × 22 mm [21,31]. The measurement scale is half the laminar flame thickness (320 μm), and the ratio of the measurement scale to the approximate Kolmogorov scale is $\lambda_m/\lambda_k \sim 20$–100. DaVis uncertainty quantification resulted in a peak velocity uncertainty that is less than 5 m/s. The centerline velocity along the axial distance is used for the analysis of the velocity profiles. Simultaneous OH^* signal is also acquired using a Photron Fastcam SAZ camera with a 50 mm and f/1.2 Nikon lens for the flame spatial location. The OH^* camera is operated at 40 kHz with a resolution 156 μm/pix [13,21,31,32,34-36].

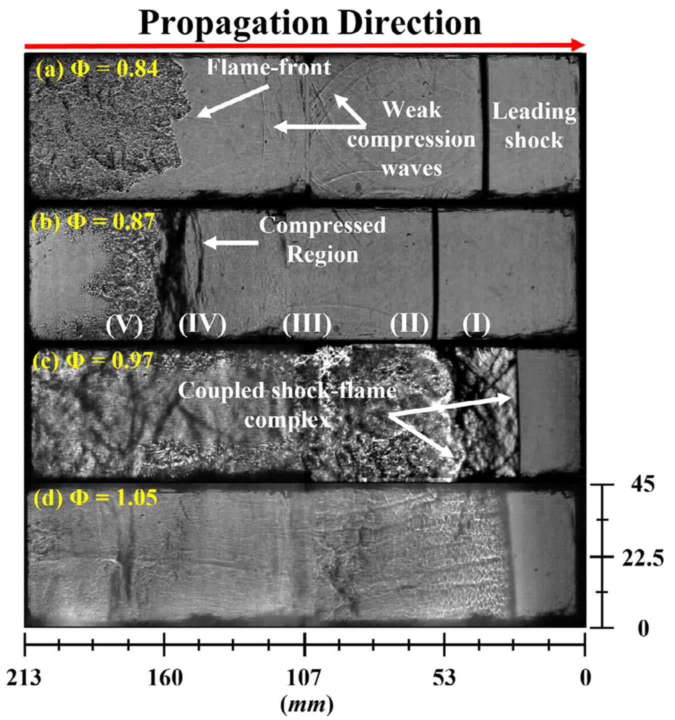

Fig. 2. Schlieren imaging (a) shockless fast deflagration, (b) shock-inducing fast deflagration, (c) coupled shock-flame complex, and (d) detonation. Measurement scale for *x*- and *y*-axes is given in mm.

3. Results and discussion

3.1. Flame characterization

In the exploration of pressure rise, various regimes - from turbulent compressible fast flames to detonations -are achieved by controlling the equivalence ratio in the range 0.84–1.05. These four regimes are classified as: shockless fast deflagration, shock-inducing fast deflagration, coupled shock-flame complex, and detonation. Figure 2 displays high-speed schlieren images of the four regimes. The images are constructed using 2 frames: a frame with the leading shock and another frame showing the post-shock flow field during the same run. The time separation between the two frames is 10 μs. Though regimes in Fig. 2 were observed in four different experiments with different equivalence ratios, these regimes can also occur in a single experiment as consecutive stages of the flame acceleration process that eventually leads to a detonation. By varying the equivalence ratio, we allowed different stages of flame acceleration to occur within the test section. This allows us to observe all these stages close to the perforated plate, without any significant influence from the channel walls that could be expected for flame evolution in longer channels. We did observe the actual flame evolution in each experiment, but it was relatively short, limited by the length of the optical window, and did not necessarily show the transition from one regime to another. Below, we often describe burning regimes as consecutive stages of flame acceleration as if it occurs in one experiment, but we refer to data from multiple experiments summarized in Figs. 2-5. The terms “shockless” and “shock-inducing” describing fast flames in Fig. 2a and 2b are not related to the leading shock, which was transferred through the perforated plate, but rather to the ability of turbulent flames to generate new shocks. For clarity, flow region labels (I) – (V) were added in Fig. 2b to denote initial state (atmospheric pressure and room temperature 297 K), shock-jump state, transient region between the leading shock and compressed region, compressed region, and flame, respectively. The flame region here is a turbulent flame brush that separates the unreacted gas in the compressed region, created by the flame itself, and the combustion products downstream of the flame. Both reactants and products are present in the flame region, and the average product concentration and gas temperature increase with distance from the compressed region.

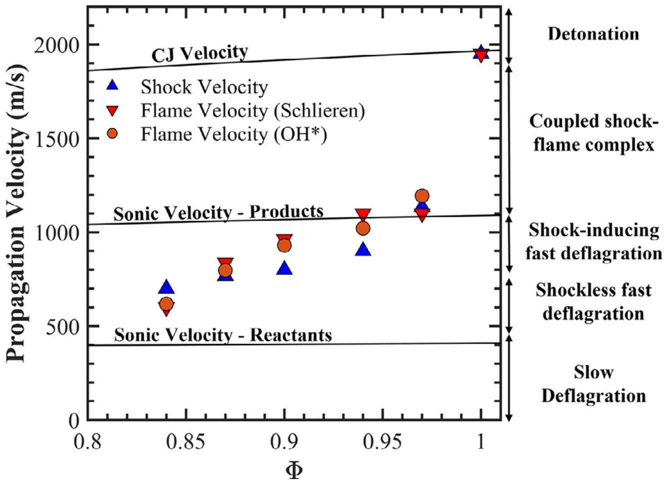

Fig. 3. Regime classification for various equivalence ratios.

The shockless fast deflagration (Fig. 2a) is characterized by a large separation between the flame and the leading shock. The flame is highly turbulent, but it generates only weak compression waves. This burning mode is akin to constant pressure deflagrations exhibited in Brayton cycle engines, which will be discussed in Section 3.3. As the flame accelerates further, it reaches the shock-inducing fast deflagration regime (Fig. 2b), where the separation distance between the leading shock and flame begin to decrease, and stronger compression waves are formed. In this regime, the turbulent flame burning speed (S_T) approaches the CJ deflagration velocity (S_{CJ}), where S_T is defined relative to the unburned material just ahead of the flame, and S_{CJ} is the maximum steady-state deflagration speed [18,21]. This results in rapid flame acceleration, which produces more compression waves to create a compressed region within and immediately ahead of the flame brush. This region of compression is essentially a new shock that is clearly detected in experiments with fast turbulent flames in this regime. Once $S_T > S_{CJ}$, the flame continues to rapidly accelerate in the runaway regime, producing shocks and strengthening the compressed region. As the compressed region develops, it becomes more pronounced and eventually it merges with the leading shock forming a coupled shock-flame complex (Fig. 2c). This regime is characterized by both the shock and flame front propagating at the product speed of sound. The flame continues to generate compression waves that quickly reach the leading shock and amplify it. Some of these waves are oblique and form a cellular-like pattern in the compressed material between the flame and the leading shock. As detonation onset occurs (Fig. 2d), CJ detonation conditions are attained, and the detonation triple point structure becomes more apparent. Note that the nascent detonation seen in Fig.2d is initially overdriven with typical cell sizes much smaller than the average cell size of = a freely propagating detonation in H_2-air mixtures at $\Phi = 1.05$, which is on the order of 15–20 mm [37,38].

By acquiring the shock and flame front propagation velocities (displacement speeds), the regimes shown in Fig. 2 can be distinguished quantitatively. Note that these propagation velocities are acquired from the schlieren measurements along with flame velocity from OH*. Figure 3 shows the regime classification based on

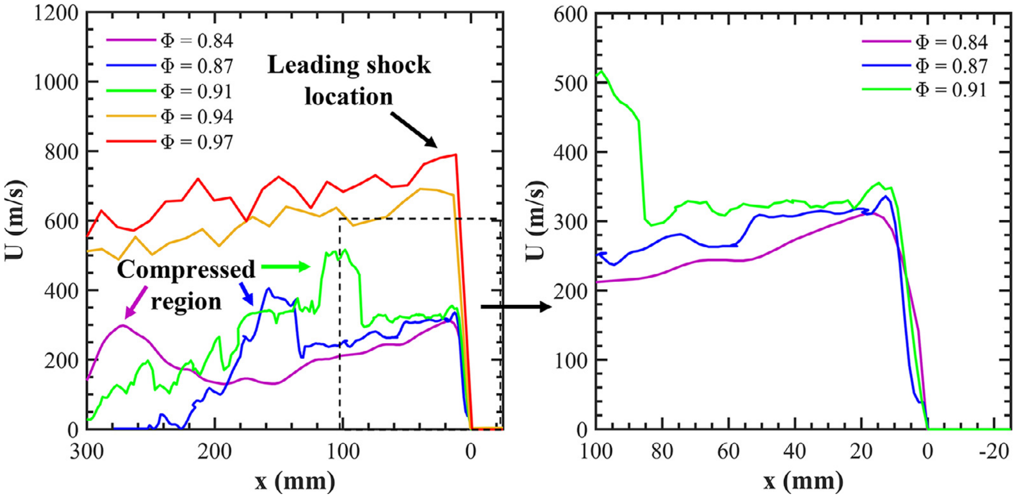

Fig. 4. Gas velocity profiles for various regimes. (Left) All profiles (Right) Zoomed in profiles near the leading shock for $\Phi = 0.84$–0.91.

the equivalence ratios, as well as shock and flame propagation velocities. For the shockless fast deflagration ($\Phi = 0.84$), the weak shock is transmitted through the last perforated plate and propagates faster than the flame. For the shock-inducing fast deflagrations ($0.85 < \Phi < 0.93$), the transmitted shock remains at some distance ahead of the flame but propagates slower than the flame. Both the flame and shock velocities increase with Φ, and the flame reaches the product sonic velocity (C_b) at $\Phi = 0.94$, where it becomes choked and the shock-flame complex begins to form. The choked flame cannot propagate any faster, but the leading shock continues to accelerate and reaches C_b at $\Phi = 0.97$. At this point, the shock-flame complex is formed. Since the shock and flame in this regime are loosely coupled and propagate with the same velocity close to C_b, below the ideal detonation velocity D_{CJ}.

3.2. Pressure and velocity evolution

Gas velocity and pressure measurements are used to quantify the local regime behavior relative to CJ conditions. The gas velocity profile (U) in Fig. 4 is taken along the centerline of each PIV frame. The shock speed (U_{sh}) is used as an anchor to calculate the spatial evolution between each frame, $\Delta x = (U_{sh} - U)\Delta t$. The centerline velocity profiles summarized in Fig. 4 for various regimes start from the leading shock that propagates from left to right. Profiles are shifted to the same shock position at $x = 0$.

The shockless and shock-inducing fast deflagrations ($\Phi = 0.84$, 0.87, 0.91) all have leading shocks propagating at approximately Mach 2 in the stationary coordinate system. The Mach number for these cases is determined from the pressure transducer measurements and confirmed with the shock tracking from the schlieren imaging in combination with the known upstream gas temperature. As the flow moves toward detonation onset, the shock strength, and thus shock velocity increases. For $\Phi = 0.84$ and 0.87, the gas velocity (U) immediately after the leading shocks tapers off and then abruptly increases again across the compressed and flame regions to 300 and 400 m/s, respectively. Both peaks (shock-jump and compressed region) for $\Phi = 0.84$ exhibit similar velocity magnitudes, however, for shock-inducing deflagrations ($\Phi = 0.87$ and 0.91), the flow velocity in the compressed region is noticeably higher than flow velocity behind the leading shock, which indicates flame acceleration. The $\Phi = 0.91$ case has a slightly stronger shockwave (Mach 2.3), and the post-shock flow velocity tapers similarly to the $\Phi = 0.84$ and 0.87 cases. The compressed region is a plateau 80 - 110 mm behind the leading shock and exhibits a larger increase in the flow velocity. When the shock-flame complex regime is observed ($\Phi = 0.94$, 0.97), the gas velocity behind the shock remains nearly constant ($U = 670 - 770$ m/s) for a short distance before gradually decreasing.

Pressure profiles shown in Fig. 5 are reconstructed from the pressure recorded by transducers as functions of time, and also using the velocity profiles shown in Fig. 4. Pressure traces are all shifted to the same location of the leading shock, and normalized by the initial pressure, i.e., 1 *atm*. For $\Phi = 0.84$, two pressure peaks are evident, indicating the leading shock and compressed region. The second peak reaches $\sim 5P_1$ at 260 mm behind the leading shock. Cases $\Phi = 0.84$, 0.87, and 0.91 exhibit similar leading shock strengths, and pressures close to the leading shock (< 50 mm) are close in all three cases. Recall that these shocks propagate at $\sim$ Mach 2, which results in a theoretical pressure ratio of $P/P_1 \sim 4.5$. This matches with the experimental shock pressure ratios shown in Fig. 5b.

The differences between cases $\Phi = 0.84$, 0.87, and 0.91 cases lie within the secondary pressure peaks generated by the stronger compression. For $\Phi = 0.87$, the compressed region reaches $\sim 6P_1$, 130 mm after the initial shock. As the leading shock intensity increases ($\Phi = 0.91$), the shock-jump pressure (Region II in Fig. 2b) becomes $5.6P_1$ (theoretical $P/P_1 \approx 6$ for Mach 2.3 shock), and compressed region also reaches a higher pressure $\sim 9P_1$ at 100 mm after the initial shock. This highlights how the compression increases when an unstable flame accelerates and catches up to the leading shock. As the fast deflagration reaches the shock-flame complex regime, the shock and compressed region peaks start to couple together ($\Phi = 0.94$, 0.97). Although these cases cannot be considered CJ detonations, there is a significant amount of pressure rise as the peaks ($14P_1$ and $20P_1$, respectively) approach the von Neumann (or ZND) pressure (theoretical $P_{vN} = 29P_1$). This indicates that for a shock-flame complex propagating at $0.5D_{CJ}$, the peak pressure can reach $0.7P_{vN}$.

3.3. Rankine-Hugoniot analysis

To characterize the pressure gain, we consider the ZND model as well as the Hugoniot curves (shock and equilibrium ones). The Rankine-Hugoniot relations derived from combining the conservation of mass, momentum, energy, and ideal-gas law include the equations of the Rayleigh line and the product Hugoniot

$$\frac{P_2/P_1 - 1}{1 - \nu_2/\nu_1} = \gamma M_1^2 \tag{1}$$

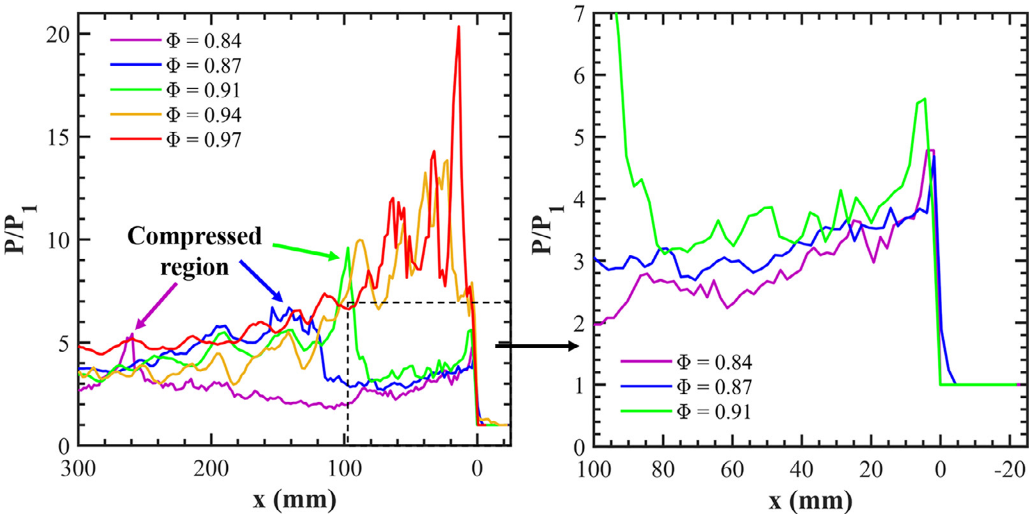

Fig. 5. Static pressure profiles for various regimes. (Left) All profiles (Right) Zoomed in profiles near the leading shock for Φ = 0.84–0.91.

$$\frac{\gamma}{\gamma-1}\left[\frac{P_2}{P_1}\frac{\nu_2}{\nu_1}-1\right]-\frac{1}{2}\left[\frac{P_2}{P_1}-\frac{\nu_2}{\nu_1}-1+\frac{P_2}{P_1}\frac{\nu_2}{\nu_1}\right]=\alpha \tag{2}$$

where M_1 is the shock Mach number, γ is the specific heat ratio, ν is the specific volume ($1/\rho$), and P is the pressure. Eqs. (1) and (2) are normalized with respect to the pre-shock state P_1 and ν_1. Eq. (2) contains the non-dimensional heat release α, which defines the inert Hugoniot ($\alpha = 0$) for unburned shock-compressed material, and equilibrium Hugoniot ($\alpha > 0$) for combustion products behind the detonation (or flame). It is important to note that Eqs. (1) and (2) place no restriction on the distance between the leading shock and the region of energy release (in a shock-flame complex or detonation).

Using the experimental velocity and pressure traces from Figs. 4 and 5, the P-ν trace can be acquired up to the maximum pressure point in the compressed region. The temperatures must be obtained in order to calculate ν behind the leading shock and in the compressed region ahead of the flame. This calculation uses a stationary coordinate system with adiabatic shock-jump conditions and isentropic relations to calculate the flow-field properties. The measured local gas velocity and gas properties are used to calculate the stagnation pressure through the isentropic relation: $^{P_o}/_{P} = \left(1+\frac{\gamma-1}{2}M^2\right)^{\gamma}/\gamma-1$, where P_o and P are the stagnation and static pressures, respectively. Note that the static properties are not affected by the choice of a reference frame, only the stagnation properties since they are dependent on velocity. Details of these calculations are explained below.

Figure 6 highlights points of interest in the schlieren image, P-ν diagram, and pressure trace for $\Phi = 0.87$. These points include the initial state (I), shock-jump state (II), transient gas between the leading shock and the compressed region (III), compressed region (IV), and the end of the flame region (V) that corresponds to completed combustion. The calculation procedure described for $\Phi = 0.87$ is applied to all the cases. For the shock-flame complex cases, only three points of interest are used (initial state, shock-jump, flame) since the compressed region and leading shock are merged.

The calculation procedure described here is also illustrated in Fig. 7. Starting with the initial state (Region I), the shock-jump conditions (Region II) are calculated using the measured shock speed, Eqs. (1) and (2), and equation of state. The resulting post-shock temperature T_2 is used to calculate the stagnation temperature behind a moving shock:

$$T_{o2}=T_2\left(1+\frac{\gamma-1}{2}\frac{U^2}{a_2^2}\right), \tag{3}$$

where U, and a_2 are the gas velocity (acquired from PIV measurements) and sound speed, respectively. Next, we calculate the transient gas conditions between the leading shock and compressed region (Region III). Note that gas in this region is assumed to be adiabatic and isentropic, thus the stagnation temperature remains nominally constant ($T_{o2} = T_{o3}$). The local temperature in Region III can then be calculated as:

$$T_3=T_{o2}-\frac{U^2}{2c_p}, \tag{4}$$

where c_p is the specific heat capacity. Although we assume isentropic flow in Region III, there are complex interactions between weak shocks, turbulence, and boundary effects which may result in non-isentropic behavior. However, the static temperature in Regions (I) – (IV) ranges from 293 to 630 K, which results in γ, c_p, and specific gas constant, R, varying by 1.6%, 4.4%, and 0.13% respectively. Thus, the gas properties γ, R, and c_p can be approximated as constant in these regions and they are computed using NASA CEA [39]. The next point of interest is the compressed region (Region IV), which follows the same calculation procedure as the leading shock using the inert shock Hugoniot. The pressure in Region (IV) is used to compute the thermodynamic properties for Regions (IV) and (V). Thus, $T_4 > T_3$, $T_{o4} > T_{o3}$, and $P_4 > P_3$. Note that there is a secondary inert Hugoniot for the compressed region, which falls close to the leading shock Hugoniot. Using the calculated temperature T and known quantities R and P, we can calculate the specific volume for all regions of interest using the ideal gas law

$$\frac{RT}{P}=\nu. \tag{5}$$

To calculate ν for the combustion products at the end of the flame region (V), the adiabatic flame temperature must be calculated. Since no temperature diagnostics are performed in this study, a CHEMKIN calculation is used to estimate the adiabatic flame temperature and heat release. Thermodynamic states in the compressed region are the initial conditions for the flame calculations and are known from experimental values (pressure) and gas-dynamic relations (temperature). We assume a constant pressure combustion process across the compressed region and flame front (P_4 = constant) and expand the products to P_5 assuming isentropic

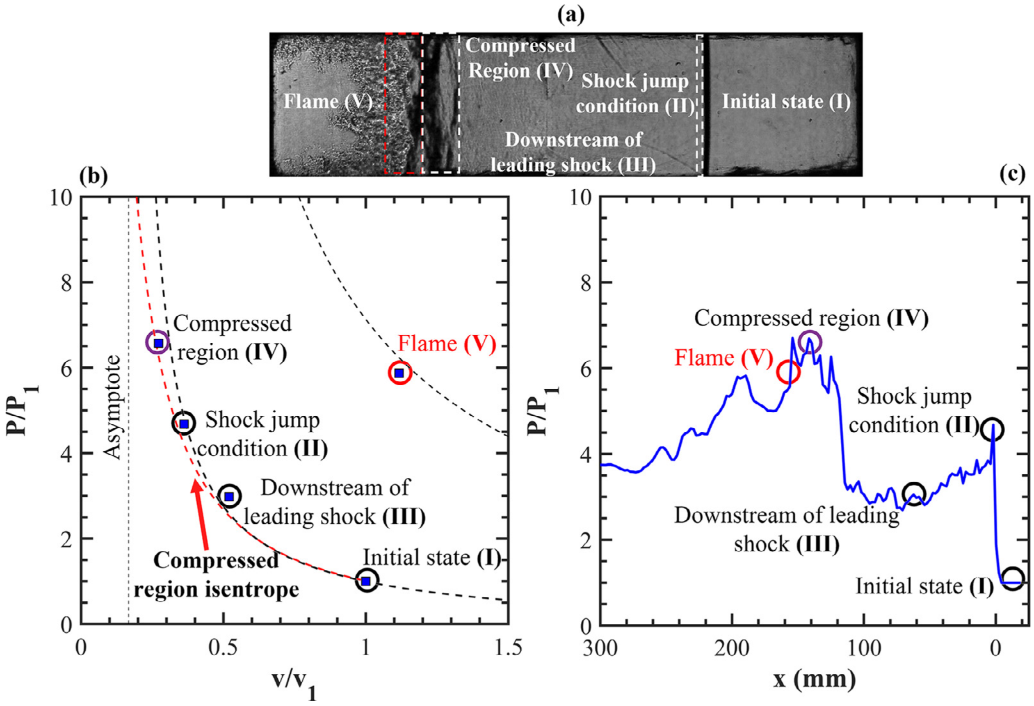

Fig. 6. Points of interest for $\Phi = 0.87$ case. (a) Schlieren highlighting regions of interest. Dashed black lines show inert and product Hugoniot curves. Dashed red line shows the isentrope. (b) P-ν diagram, (c) pressure trace. (For interpretation of the references to color in this figure legend, the reader is referred to the web version of this article.).

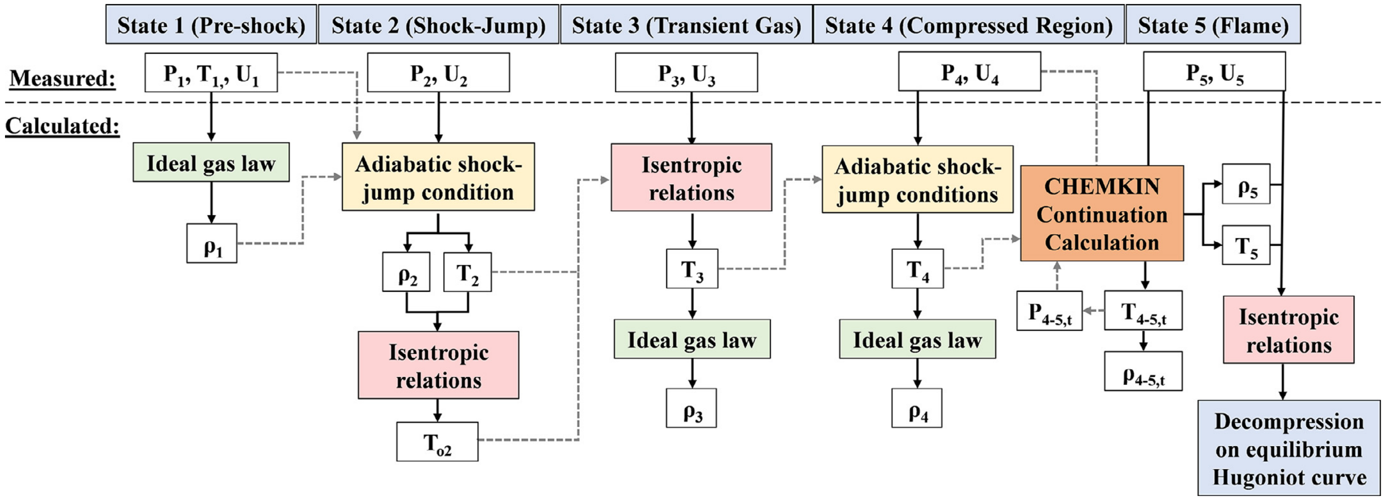

Fig. 7. Flowchart outlining calculation procedure of thermodynamic properties for every state.

flow in the products ($P\nu^{\gamma}$ = constant). Since combustion results in a significant temperature increase from Region (IV) to (V), γ, R, and c_p will not remain constant (γ and R decrease while c_p increases). We use the product γ, R, and c_p values to calculate the Region (V) properties. This produces the same adiabatic flame temperature as the Chemkin Continuation method used to compute the P-v trajectory between states IV and V as described below ($<$ 1% difference). Using this assumption, we can compute the equilibrium Hugoniot conditions from finding the adiabatic flame temperature [38]. Note that this calculation assumes no heat or energy losses. For reference, Table 1 shows the intermediate thermodynamic properties for Regions (I) – (V) which have been transformed back into the lab coordinate frame.

Figure 8 displays the static and stagnation P-ν states overlapped onto the theoretically calculated Hugoniot curves. The ideal ZND markers are the theoretically calculated von Neumann and CJ values. Similar to Fig. 5, pressure is normalized with the initial pressure (P_1) and ν is normalized with the specific volume (ν_1) of unreacted gas ahead of the shock. In Fig.8a, horizontal dashed lines represent the CJ pressure ratio from $\Phi = 0.84$ to $\Phi = 0.97$, and the markers represent the regions of interest shown in Fig. 6. From initial observations, the P-ν curves show a strong agreement with the theoretical Hugoniot curves. For a shockless fast deflagration ($\Phi = 0.84$), flame-driven compression results in a new peak pressure state P_4, for which the point falls just outside of the initial inert Hugoniot and represents an additional shock adiabat (or secondary Hugoniot); this behavior is similar for the $\Phi = 0.87$ and 0.91 case. In the $\Phi = 0.84$ and 0.87 cases, the pressures in the compressed region and at the end of the flame region are almost the same, which indicates a constant-pressure combustion behind the secondary shock. For a stronger shock-induced fast deflagration ($\Phi = 0.91$), the pressure gap between the compressed region

Table 1

Thermodynamic properties at regions of interest for $\Phi = 0.87$. Static and stagnation pressure uncertainties are ±0.17 atm and ±0.078 atm, respectively.

	Experimental values		*Calculated values*			
	P_{st} **(atm)**	U **(m/s)**	T **(K)**	v **(m^3/kg)**	P_o/P	P_o **(atm)**
Initial state (I)	1.00	0	297	1.13	1.00	1.00
Shock-jump state (II)	4.68	320	516	0.41	1.31	6.13
Transient gas (III)	2.36	250	423	0.58	1.21	2.86
Compressed region (IV)	6.57	360	538	0.31	1.47	9.66
Flame (V)	5.87	330	2465	1.26	1.05	6.16

Where P_{st} and P_o are the static and stagnation pressures, respectively.

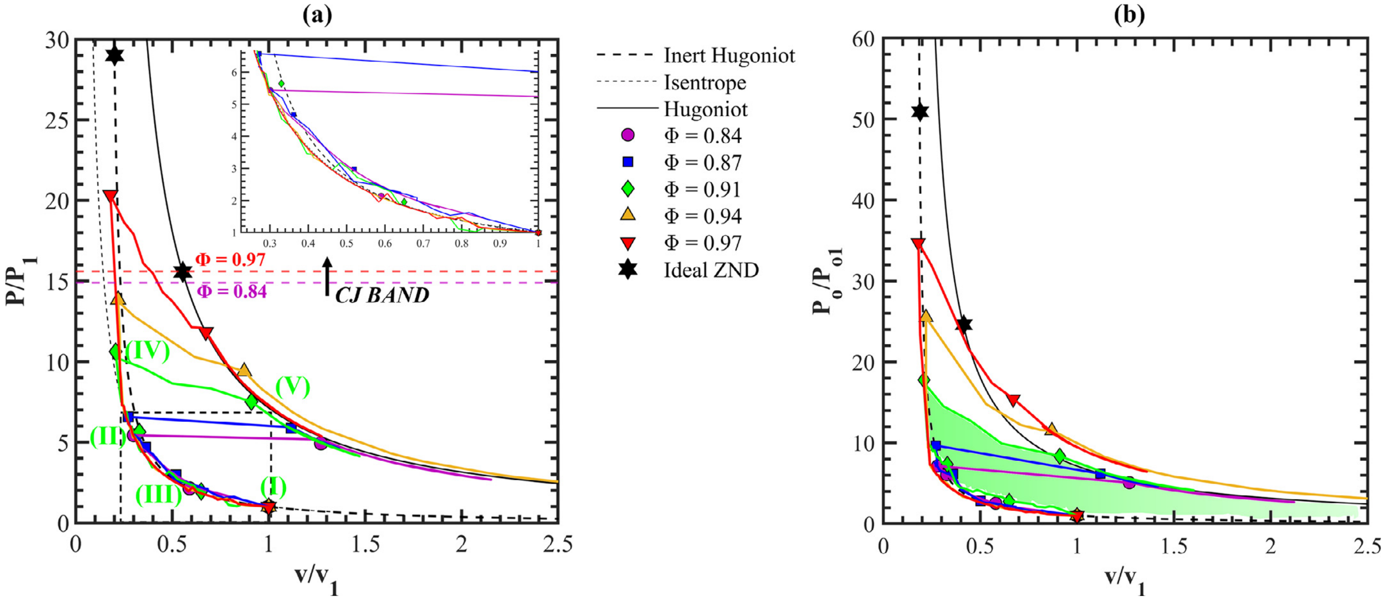

Fig. 8. P-v evolution on the Rankine-Hugoniot diagram. (a) Static pressure. Dashed box indicates zoomed in area (b) Stagnation pressure. Shaded area indicates network for $\Phi = 0.91$.

and the end of the flame begins to grow because the accelerating flame is generating more compression. For these regimes, flame-driven pressure gain is dependent upon a combination of the leading shock and turbulent compressed region.

As the material burns inside the flame brush downstream of the compressed region, the pressure and density decrease. On the P-v diagram, this process is shown as a line connecting state (IV) close to the inert Hugoniot and state (V) on the equilibrium Hugoniot. Pressures along this line are measured every 1 μs, which corresponds to the operating frequency of pressure transducers. The actual pressure transducer frequency of 4 μs is interpolated to 1 μs to provide a higher resolution for the CHEMKIN calculation. The specific volumes are calculated using the CHEMKIN Continuation method, which includes a constant pressure combustion calculation for a time increment of 1 μs followed by an adiabatic expansion to the next measured pressure point. We start with the unreacted state IV, namely corresponding pressure, and continue the incremental combustion and expansion steps until the pressure is expanded to state V, and the combustion is completed. The fluctuations in Fig. 8 are due to oscillations in experimental pressure traces. Note that the adiabatic flame temperature is minimally affected by using state IV or V as the initial pressure (< 1% difference).

As flame driven compression increases, the burning mode transitions to a shock-flame complex regime ($\Phi = 0.94, 0.97$), where the flame is choked and it continually issues strong compression waves, which couple with the leading shock. The peak pressure state shifts from the secondary Hugoniot towards to the initial shock Hugoniot. This indicates the coalescence between the compressed region and the leading shock. The growth in pressure difference between the post-shock gases and post-flame products also illustrates how flame-driven compression changes the combustion process from constant pressure (shockless fast deflagration) to a quasi-ZND cycle (shock-flame complex).

When the gas kinetic energy is factored in, we observe a noticeable increase in stagnation pressures at the higher equivalence ratios as shown in Fig. 8b. Note that the stagnation pressures are calculated in the reference frame analogous to a PDE, where the gas velocity ahead of the leading shock is zero. The $\Phi = 0.84$ and 0.87 cases show a minimal increase in P_o compared to the static pressure P as the gas velocity contribution is minimal. Once flame-driven compression increases, the compressed region gas velocity increases leading to the overall increase in stagnation pressure. The pressure jumps from, $P = 11P_1$ to $P_o = 18P_1$ for $\Phi = 0.91$ (since the initial gas velocity $U = 0$, then $P_1 = P_{o1}$), $P = 14P_1$ to $P_o = 25P_1$ for $\Phi = 0.94$ and $P = 20P_1$ to $P_o = 35P_1$ for $\Phi = 0.97$. The stagnation P-v diagram can also be used to calculate the network produced. The network is calculated by evaluating the integral, or area bounded by the Hugoniot curves and the Rayleigh line for each case. For the shock-flame complex cases, products expand isentropically along Pv^{γ} = constant rather than the equilibrium Hugoniot. Thus, we will compute the network for both scenarios: along the equilibrium isentrope as shown in Fig. 8b, and assuming these cases will expand along the equilibrium Hugoniot.

The isentropic expansion is computed using the frozen sound speed assumption where the reactions have been completed, and

Table 2
Comparison of various burning mode efficiencies with respect to ZND cycle. $\Phi = 1.05$ for ZND case.

Φ	Burning Mode	P_{o4}/P_{o1} (Region IV)	*Net Work* (MJ/kg)	η_{ZND}	η_{th}
0.84	Shockless deflagration	7.1	1.24	0.52	0.40
0.87	Shock-inducing deflagration	9.6	1.32	0.55	0.41
0.91	Shock-inducing deflagration	17.7	1.71	0.69	0.47
0.94	Weak shock-flame complex	25.5	1.78 (2.10)	0.74 (0.88)	0.50 (0.59)
0.97	Shock-flame complex	34.8	1.94 (2.49)	0.83 (1.04)	0.54 (0.68)
1.05	ZND Detonation	50.9	2.40	1.00	0.64

no further composition changes occur. The pressure, specific volume, and specific heat ratio at state V are used to calculate the isentrope constant ($P\nu^{\gamma}$ = constant) which is then used along with the measured experimental pressures to compute the local specific volume from state V to $P/P_1 = 1$. Note that this assumption does not account for the possibility of reactions transpiring from state V to P/P1 = 1. It is expected that there will be differences between the isentropic expansion and the equilibrium Hugoniot since the former is based on the frozen assumption and the latter is based on theoretical heat release. The heat release could result in further pressure expansion and a decompression profile that falls between the isentrope and the equilibrium Hugoniot curves. This would decrease the work and thermal efficiency values shown in Table 2. This is shown in the $\Phi = 0.94$ and 0.97 cases where the frozen assumption results in thermal efficiencies of 59% and 68% respectively. If reactions continuously occur, the thermal efficiencies would likely be closer to 50% and 54%. The weaker cases show minimal difference between the product isentrope and equilibrium Hugoniot, therefore, we only calculate the network along the equilibrium Hugoniot. As an example, Fig. 8b shows a lightly shaded region highlighting the area of interest for one case. For consistency, $P/P_1 = 1$ on the equilibrium Hugoniot is used as the maximum ν value for all cases. The minimum ν value will correspond to the maximum pressure point for each case on the inert Hugoniot curve.

We assume that the expansion from the ZND point, or maximum pressure point on the inert Hugoniot for each case, is where the useful work starts. The Hugoniot and Rayleigh line data points are imported into Wolfram Mathematica and numerically integrated to calculate these values. The heat release is calculated for every Φ to compute thermal efficiency. The burning mode, network, efficiency with respect to the ideal ZND work (η_{ZND} = net work / ZND network), and thermal efficiency (η_{th} = net work / heat release) is shown in Table 2. For $\Phi = 0.94$ and 0.97, the values in parenthesis indicate the work and efficiencies calculated using isentropic expansion rather than the equilibrium Hugoniot expansion. The work and thermal efficiency versus compressed region stagnation pressure ratio are plotted in Fig. 9 to show how an increase in stagnation pressure brings the cycle efficiency closer to the ideal ZND efficiency. It is important to note that we compare efficiencies of various burning regimes observed in our facility. Since the facility produces CJ detonations at $\Phi = 1.05$, we compare the five cases to the ZND case at a constant $\Phi = 1.05$. If we were to compare the $\Phi = 0.84$ shockless deflagration case to a $\Phi = 0.84$ ZND case, the efficiency and η_{th} would be slightly higher. Thus, the efficiency and η_{th} values shown in Table 2 can be considered conservative values since they are all relative to a $\Phi = 1.05$ ZND detonation.

Since the ZND case is ideal, η_{ZND} is denoted as 100% efficient with respect to itself. The shockless deflagration and weak shock-inducing deflagration cases only show 52% and 55% work efficiency with respect to an ideal ZND cycle, which is expected since they behave closer to constant pressure combustion cycles. When the flame propagation velocity nears C_b ($\Phi = 0.91$ – stronger shock-inducing deflagration), P_{o4}/P_{o1} is nearly doubled from the weak shock-inducing deflagration case, and efficiency increases to 69%. Once the flame becomes choked, η_{ZND} increases to 74% and 83% in the shock-flame complex regimes if we assume expansion along the equilibrium Hugoniot. When the products are expanded along the equilibrium isentrope, there is a significant increase to 88% and 104% efficiency with respect to the ZND cycle. Since the isentrope originating at state V lies above the expansive branch of the equilibrium Hugoniot, the network is expected to be larger when the integral is computed. Actual combustion products will not continuously expand isentropically until $P/P_1 = 1$ when losses and 3-D effects are taken into consideration. Expansion along the equilibrium Hugoniot is more indicative of actual combustion products.

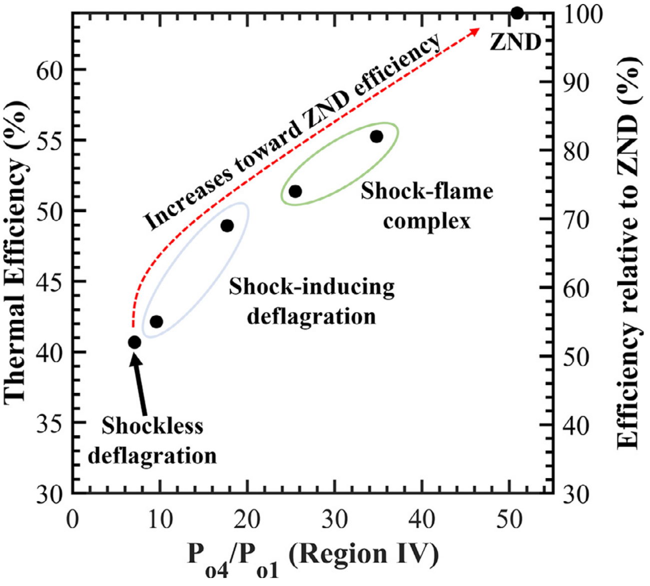

Fig. 9. Cycle efficiency versus stagnation pressure ratio of compressed region.

Furthermore, by calculating η_{th}, we can compare thermal cycle efficiency values between static and stagnation pressures. Kailasanath [1] uses static pressures and reports η_{th} values of 27% for constant pressure combustion cycle and 49% for a detonation cycle. Note that these thermal efficiencies were computed assuming the same heat release between the two cases although detonations exhibit a larger heat release than a constant pressure combustion cycle. Zhou et al. [40] also use static pressures and report a similar ZND thermal efficiency of 51%, while Vutthivithayarak et al. [22] use stagnation pressures and compute $\eta_{th} = 70\%$. Thermal efficiencies reported by Kailasanath et al., Zhou et al., and Vutthivithayarak et al. are based on the ZND combustion process, thus it is reasonable to compare their reported values. We calculate thermal efficiencies using stagnation pressures and find $\eta_{th} = 64\%$ for the ideal ZND cycle, which is approximately 13% more than the cycle efficiency based on static pressures.

This emphasizes the importance of the gas velocity contribution in the pressure gain process. The $\Phi = 0.84$, 0.87, and 0.91 cases exhibit cycle efficiencies based on stagnation pressures in the range

η_{th} = 40–47%. Although the $\Phi = 0.84$ case has 40% thermal efficiency using stagnation pressure, it would likely be closer to 27% for a constant pressure combustion cycle if it were to be computed using static pressure. For $\Phi = 0.94$ and 0.97 (shock-flame complexes), $\eta_{th} = 50\%$ and 54%, respectively. As before, the shock-flame complex thermal efficiencies are higher when expanded along the isentrope, $\eta_{th} = 59\%$ and 68%. When expanded along the equilibrium Hugoniot, these efficiencies are similar to the ideal ZND thermal efficiency values reported by Kailasanath et al. and Zhou et al. meaning the P_o thermal efficiency of a shock-flame complex may be similar to the static pressure thermal efficiency of an ideal ZND cycle. This also highlights how shock-flame complexes (or decoupled detonations) produce a significant amount of pressure gain as well as thermal and work efficiency with respect to an ideal ZND cycle before the CJ detonation state is attained.

4. Conclusion

This work presented the analysis of pressure evolution for various combustion regimes, from propagating turbulent shockless deflagrations to a shock-flame complex using the Rankine-Hugoniot diagram. High-speed schlieren, PIV, and pressure measurements were used to observe and characterize the flow-field behavior. The pressure, velocity, and optical measurements agree in terms of spatial locations of the shock and compressed region. The four regimes studied were: shockless fast deflagration, shock-inducing fast deflagration, coupled shock-flame complex, and detonation. These fast flames regimes between constant pressure and constant volume burning modes exhibited various levels of pressure gain depending on the level of shock-flame separation and strength of flame-driven compression. We analyze these combustion regimes using the pressure-specific volume diagram and compute the efficiency of the corresponding thermodynamic cycles using stagnation pressures. For the ideal ZND cycle, this approach gives $\eta_{th} = 64\%$. At lower degrees of compressibility, the shockless deflagration exhibits behavior similar to a constant pressure cycle, resulting in $\eta_{ZND} = 52\%$ and $\eta_{th} = 40\%$. For shock-inducing fast deflagrations, two distinct pressure peaks were formed as a result of the leading shock and a flame-driven compression front. As the flame becomes choked and coupled with the leading shock, compression grows stronger and pressure gain increases. For this regime, pressure gain is dependent upon both the strength of the turbulent compressed region and the leading shock. When the compressed region and the leading shock merge, a shock-flame complex forms, and the cycle efficiency reaches up to 83% of the ideal ZND cycle efficiency and 54% thermal efficiency. These results demonstrate how a substantial pressure gain can be achieved through shock-flame complexes (decoupled detonations).

Declaration of Competing Interest

None.

Acknowledgments

The authors acknowledge the Air Force Office of Scientific Research support under award 19RT0258/FA9550-19-0322 by Program Manager Dr. Chiping Li and the National Science Foundation Award #1914453. We would also like to thank Dr. Wilmer Flores for his valuable discussion.

References

[1] K. Kailasanath, Review of propulsion applications of detonation waves, AIAA J. 38 (2000) 1698–1708.

[2] D. Schwer, K. Kailasanath, Numerical investigation of the physics of rotating-detonation-engines, Proc. Combust. Inst. 33 (2011) 2195–2202.

[3] K.D. Rein, S. Roy, S.T. Sanders, A.W. Caswell, F.R. Schauer, J.R. Gord, Measurements of gas temperatures at 100kHz within the annulus of a rotating detonation engine, Appl. Phys. B 123 (2017) 88.

[4] M. Fotia, J. Hoke, F. Schauer, Study of the ignition process in a laboratory scale rotating detonation engine, Exp. Therm. Fluid Sci. 94 (2018) 345–354.

[5] D. Depperschmidt, R. Miller, J. Tobias, M. Uddi, A.K. Agrawal, J.B. Stout, Time-resolved PIV diagnostics to measure flow field exiting methane-fueled rotating detonation combustor, AIAA Scitech Forum, 2019 Paper No. 2019-1514.

[6] J. Sosa, K.A. Ahmed, R. Fievisohn, J. Hoke, T. Ombrello, F. Schauer, Supersonic driven detonation dynamics for rotating detonation engines, Int. J. Hydrog. Energy 44 (2019) 7596–7606.

[7] B.A. Rankin, J.R. Codoni, K.Y. Cho, J.L. Hoke, F.R. Schauer, Investigation of the structure of detonation waves in a non-premixed hydrogen–air rotating detonation engine using mid-infrared imaging, Proc. Combust. Inst. 37 (2019) 3479–3486.

[8] T.M. Ombrello, C.D. Carter, C.-J. Tam, K.Y. Hsu, Cavity ignition in supersonic flow by spark discharge and pulse detonation, Proc. Combust. Inst. 35 (2015) 2101–2108.

[9] Q. Zhang, K. Wang, R. Dong, W. Fan, W. Lu, Y. Wang, Experimental research on propulsive performance of the pulse detonation rocket engine with a fluidic nozzle, Energy 166 (2019) 1267–1275.

[10] J.K. Lefkowitz, P. Guo, T. Ombrello, S.H. Won, C.A. Stevens, J.L. Hoke, F. Schauer, Y. Ju, Schlieren imaging and pulsed detonation engine testing of ignition by a nanosecond repetitively pulsed discharge, Combust. Flame 162 (2015) 2496–2507.

[11] K.D. Rein, S. Roy, S.T. Sanders, A.W. Caswell, F.R. Schauer, J.R. Gord, Multi-species absorption spectroscopy of detonation events at 100kHz using a fiber-coupled, time-division-multiplexed quantum-cascade-laser system, Appl. Opt. 55 (2016) 6256–6262.

[12] T.A. Kaemming, D.E. Paxson, Determining the pressure gain of pressure gain combustion, 2018 Joint Propulsion Conference, 2018 Paper No. 2018-4567.

[13] J. Chambers, K.A. Ahmed, L.R. ONeill, A. Poludnenko, V.N. Gamezo, Evidence of pressure build-up in H2-air fast flames for deflagration-to-detonation, AIAA Scitech Forum, 2019 Paper No. 2019-0189.

[14] C.A. Nordeen, D. Schwer, F. Schauer, J. Hoke, T. Barber, B. Cetegen, Thermodynamic model of a rotating detonation engine, Combust. Explos. Shock Waves 50 (2014) 568–577.

[15] T. Sato, S. Voelkel, V. Raman, Analysis of detonation structures with hydrocarbon fuels for application towards rotating detonation engines, Joint Propulsion Conference, 2018 Paper No. 2018-4965.

[16] A.Y. Poludnenko, The role of flame-generated turbulence in the deflagration–to-detonation transition, 26th International Colloquium on the Dynamics of Explosions and Reactive Systems, 2017 Paper No. ICDERS 2017-1247.

[17] B.T. Chu, Mechanism of Generation of Pressure Waves At Flame Fronts, NACA TN (1956), p. 3683.

[18] A.Y. Poludnenko, Pulsating instability and self-acceleration of fast turbulent flames, Phys. Fluids 27 (2015) 014106.

[19] A.Y. Poludnenko, E.S. Oran, The interaction of high-speed turbulence with flames: global properties and internal flame structure, Combust. Flame 157 (2010) 995–1011.

[20] A.Y. Poludnenko, T.A. Gardiner, E.S. Oran, Spontaneous transition of turbulent flames to detonations in unconfined media, Phys. Rev. Lett. 107 (2011) 054501.

[21] A.Y. Poludnenko, J. Chambers, K. Ahmed, V.N. Gamezo, B.D. Taylor, A unified mechanism for unconfined deflagration-to-detonation transition in terrestrial chemical systems and type Ia supernovae, Science 366 (2019).

[22] R. Vutthivithayarak, E. Braun, F. Lu, On thermodynamic cycles for detonation engines, 28th International Symposium on Shock Waves, 2012.

[23] A. Oppenheim, Gasdynamic analysis of the development of gaseous detonation and its hydraulic analogy, Symp. (Int.) Combust. 4 (1953) 471–480.

[24] Y.K. Troshin, The generalized Hugoniot adiabatic curve, Symp. (Int.) Combust. 7 (1958) 789–798.

[25] D. Schwer, K. Kailasanath, Numerical investigation of rotating detonation engines, Joint Propulsion Conference, 2010 Paper No. AIAA 2010-6880.

[26] I.B. Dunn, K. Thurmond, K.A. Ahmed, S. Vasu, Exploration of measuring pressure gain combustion within a rotating detonation engine, Joint Propulsion Conference, 2018 Paper No. 2018-4566.

[27] C.L. Journell, R.M. Gejji, I.V. Walters, A.I. Lemcherfi, C.D. Slabaugh, J.B. Stout, High-speed diagnostics in a natural gas–air rotating detonation engine, J. Propul. Power 36 (2020) 498–507.

[28] M.J. McClearn, F.R. Schauer, R. Huff, M.D. Polanka, J.L. Hoke, M. Fotia, A disk rotating detonation engine part 2: operation, AIAA Aerospace Sciences Meeting, 2018 Paper No. 2018-1607.

[29] D.R. Cuppoletti, T. Ombrello, K.D. Rein, Detonation amplification and attenuation through geometric area expansion, AIAA Scitech Forum, 2019 Paper No. 2019-1012.

[30] D. Cuppoletti, T. Ombrello, K. Rein, Energy coupling mechanism for pulse detonation ignition of a scramjet cavity, Proc. Combust. Inst. 37 (2019) 3453–3460.

[31] J. Sosa, J. Chambers, K.A. Ahmed, A. Poludnenko, V.N. Gamezo, Compressible turbulent flame speeds of highly turbulent standing flames, Proc. Combust. Inst. 37 (2019) 3495–3502.

[32] J. Chambers, K. Ahmed, A. Poludnenko, Exploration of turbulence driven deflagration to detonation of fast flames, 26th ICDERS, 2017.

[33] S.S. Dammati, Y. Kozak, C. Rising, J. Reyes, K. Ahmed, A.Y. Poludnenko, Numerical investigation of the accuracy of particle image velocimetry technique in gas-phase detonations, Proc. Combust. Inst. 38 (2021) 3671–3681.

[34] H.M. Chin, J. Chambers, J. Sosa, K.A. Ahmed, Quantification of pressure gain in turbulent fast flames for deflagration-to-detonation, AIAA Scitech Forum, 2020 Paper No. 2020-0442.

[35] H.M. Chin, J. Chambers, J. Sosa, K.A. Ahmed, A. Poludnenko, V.N. Gamezo, The sonic line of a propagating detonation wave, AIAA Scitech Forum, 2020 Paper No. AIAA 2020-0444.

[36] J. Chambers, K.A. Ahmed, Investigation of flame regimes for flame acceleration to detonation, Joint Propulsion Conference, 2018 Paper No. AIAA 2018-4967.

[37] M. Kaneshige, J.E. Shepherd, Detonation database, GALCIT, 1997 Tech. Rep. FM97-8.

[38] J.H. Lee, The detonation phenomenon, Cambridge University Press, New York, 2008.

[39] B.J. McBride, S. Gordon ,Computer program for calculation of complex chemical equilibrium compositions and applications II, user's manual and program description NASA Report, 1996 Report No. NASA RP-1311-P2.

[40] R. Zhou, J.-.P. Wang, Numerical investigation of flow particle paths and thermodynamic performance of continuously rotating detonation engines, Combust. Flame 159 (2012) 3632–3645.